

Automated 3-D Retinal Layer Segmentation of Macular Optical Coherence Tomography Images with Serous Pigment Epithelial Detachments

Fei Shi, Xinjian Chen*, Heming Zhao, Weifang Zhu, Dehui Xiang, Enting Gao, Milan Sonka,

Fellow, IEEE, and Haoyu Chen

Abstract—Automated retinal layer segmentation of optical coherence tomography (OCT) images has been successful for normal eyes but becomes challenging for eyes with retinal diseases if the retinal morphology experiences critical changes. We propose a method to automatically segment the retinal layers in 3-D OCT data with serous retinal pigment epithelial detachments (PED), which is a prominent feature of many chorioretinal disease processes. The proposed framework consists of the following steps: fast denoising and B-scan alignment, multi-resolution graph search based surface detection, PED region detection and surface correction above the PED region. The proposed technique was evaluated on a dataset with OCT images from 20 subjects diagnosed with PED. The experimental results showed that: (1) the overall mean unsigned border positioning error for layer segmentation is $7.87 \pm 3.36 \mu\text{m}$, and is comparable to the mean inter-observer variability ($7.81 \pm 2.56 \mu\text{m}$). (2) the true positive volume fraction (TPVF), false positive volume fraction (FPVF) and positive predicative value (PPV) for PED volume segmentation are 87.1%, 0.37% and 81.2%, respectively; (3) the average running time is 220s for OCT data of $512 \times 64 \times 480$ voxels.

Index Terms—Retinal layer segmentation, pigment epithelium detachment (PED), optical coherence tomography (OCT)

Manuscript received July 18, 2014; revised September 10, 2014; accepted September 15, 2014. This work was supported in part by the National Basic Research Program of China (973 Program) under Grant 2014CB748600, and in part by the National Natural Science Foundation of China (NSFC) under Grant 81371629, 6140293, 61401294, 81401451 and 81401472. *Asterisk indicates corresponding author.*

F. Shi, X. Chen, H. Zhao, W. Zhu, D. Xiang and E. Gao are with the School of Electronics and Information Engineering, Soochow University, Suzhou, China (email: shifei, xjchen, hmzhao, wfzhu, xiangdehui@suda.edu.cn, gaoenting@foxmail.com).

M. Sonka is with the Department of Electrical and Computer Engineering, the Department of Radiation Oncology, and the Department of Ophthalmology and Visual Sciences, The University of Iowa, Iowa City, IA 52242 USA (e-mail: milan-sonka@uiowa.edu).

H. Chen is with Joint Shantou International Eye Center, Shantou University and the Chinese University of Hong Kong, Shantou, China (email: drchenhaoyu@gmail.com).

Copyright (c) 2010 IEEE. Personal use of this material is permitted. However, permission to use this material for any other purposes must be obtained from the IEEE by sending a request to pubs-permissions@ieee.org.

I. INTRODUCTION

OPTICAL coherence tomography (OCT), a noninvasive, non-contact scan of the retina that shows its cross-sectional profile, has been used clinically for assessment of a variety of ocular diseases, such as glaucoma, diabetic macular edema (DME), and age-related macular degeneration (AMD). Recently introduced spectral domain (SD) OCT produces high-resolution real 3-D volumetric scan of the retina, and most of the anatomical layers of the retina can be visualized. Many methods have been proposed for automated retinal layer segmentation of SD-OCT images of normal eyes, and have obtained satisfactory results [1-15]. Fig. 1 shows a macular centered OCT B-scan (axial view) of a normal eye and the 11 surfaces that define 10 retinal layers, segmented using the Iowa Reference Algorithm [14]. The surfaces are numbered 1 to 11 from top to bottom. The retinal layers thus defined are nerve fiber layer (NFL), ganglion cell layer (GCL), inner plexiform layer (IPL), inner nuclear layer (INL), outer plexiform layer (OPL), outer nuclear layer & inner segment layer (ONL + ISL), connecting cilia (CL), outer segment layer (OSL), Verhoeff's membrane (VM), and retinal pigment epithelium (RPE).

Layer segmentation methods designed for normal retinas have also been successfully applied to retinas with certain types of diseases, such as glaucoma [11,12,16] and multiple sclerosis [13], or other diseases at an early stage, when no dramatic change in the layer structure happens. However, they usually experience difficulty when additional structures exist, such as intraretinal cysts, subretinal or sub-RPE fluid in DME and wet AMD. In these cases, layer segmentation becomes challenging due to the following two reasons. First, the morphological features of each layer may vary greatly, and some constraints such as layer smoothness and thickness may not apply as in the normal case. Secondly, the degradation of image quality caused by abnormalities may affect the segmentation performance. Therefore, new methods that can segment retinas with abnormalities are needed for quantitative analysis of these diseases. The significance of layer segmentation in pathological study and clinical practice lies in the following two aspects. First, with the segmentation information, the morphological and optical features of each individual layer and their difference from normal ones can be analyzed, which can improve the understanding of the disease progression and also can facilitate

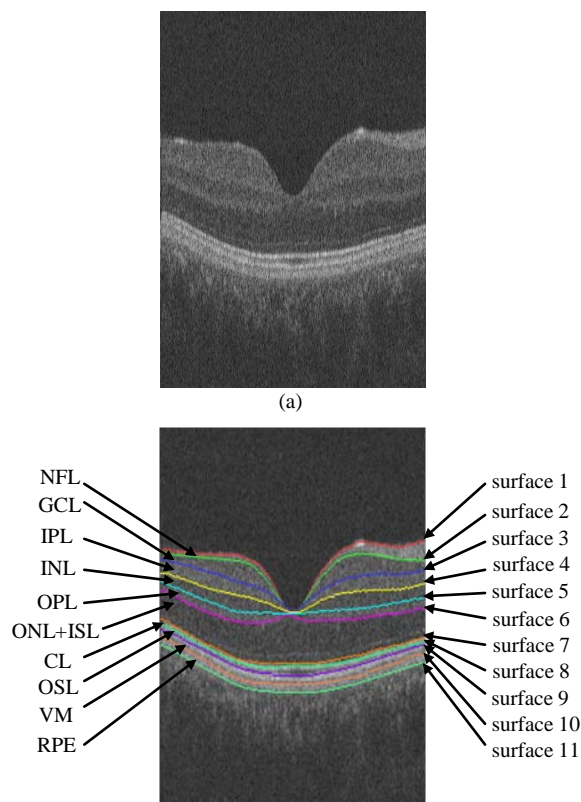


Fig. 1. OCT image of a normal eye and the 11 surfaces defining 10 retinal layers. (a) B-scan image of OCT volume, obtained using Topcon 3D-OCT 1000. (b) The 11 surfaces overlaid on the OCT image.

diagnosis. Secondly, layer segmentation can localize the abnormal regions and serve as a pre-processing step for automated detection and analysis of the abnormalities [17-23].

In this paper, we focus on segmentation for retinas with serous pigment epithelium detachments (PED's), which is associated with sub-RPE fluid and RPE deformation. We report a fully automated, unsupervised 3-D layer segmentation method for macular-centered OCT images with serous PED's. In this work, layer segmentation and abnormal region segmentation are effectively integrated, where the position of layers and regions serve as constraints for each other.

PED is a prominent feature of many chorioretinal disease processes, including AMD, polypoidal choroidal vasculopathy, central serous chorioretinopathy, and uveitis [24, 25]. PED's can be classified as serous, fibrovascular, or drusenoid. Study shows that patients diagnosed with serous PED associated with AMD frequently have co-existing choroidal neovascularization (CNV), or have a higher risk of developing CNV, which can eventually cause severe visual acuity loss [25, 26]. PED is routinely diagnosed by 2-D imaging techniques such as fluorescein angiography (FA) and indocyanine green angiography (ICGV). More recently, SD-OCT offers a means to show the cross-sectional morphologic characteristics of PED and to provide more detailed anatomic assessment. In OCT images, the RPE appears as a bright layer, and serous PED appears as a localized, relatively pronounced dome-shaped elevation of the RPE layer, as shown in Fig.2.

There were several reported methods related to segmentation of OCT images with PED's or other abnormalities. Penha *et al.*

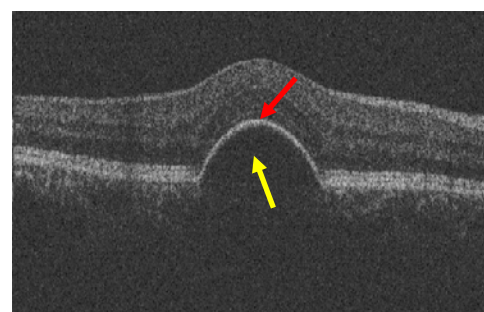


Fig. 2. An OCT B-scan showing PED. The red arrow indicates the elevated RPE and the yellow arrow indicates the detached region.

[17] utilized the software on the commercially available Cirrus SD-OCT to detect the RPE and a method proposed by Gregori *et al.* [18] to create a virtual RPE floor free of any deformations. The combination of these algorithms permitted the detection of PED's. The same algorithm was also used to study drusen associated with AMD [18]. Ding *et al.* [19] detected the top and bottom surfaces of the retina as constraints for subretinal and sub-RPE fluid detection. Chen *et al.* [20] segmented the fluid-associated abnormalities associated with AMD using a combined graph-search -graph-cut (GS-GC) method. The abnormal region was detected together with two auxiliary surfaces. Dufour *et al.* [21] detected six surfaces using graph-search based method with soft constraints [7] in OCT images with drusen. Quellec *et al.* [22] segmented eleven surfaces in OCT images with fluid-associated abnormalities. However, all these works focused on region segmentation only. In [17-20], only two or three surfaces were detected and served as constraints for the region segmentation purpose. In [21, 22], more surfaces were detected and their position information was utilized to indicate or detect retinal abnormalities. For all works reported in [17-22], no evaluation of layer segmentation accuracy was given.

In comparison with the existing methods, the proposed method achieves the following goals:

- The retinal OCT image with PED's is segmented into all discernible layers.
- Both layer segmentation and abnormal region segmentation are performed and high accuracy is achieved.
- The method is designed for retinas with serous PED's, but it also maintains good performance for normal retinas.

II. METHOD

A. Method Overview

The proposed method consists of pre-processing, layer segmentation and region segmentation (Fig.3). In pre-processing, the OCT scans are first denoised using fast bilateral filtering. Then the B-scans are aligned to correct distortion caused by the eye movement. During layer segmentation, a multi-resolution graph-search method [3, 16] is utilized. Surfaces 1-6 are first detected. Then the elevated RPE floor (surface 11) and the estimated normal RPE floor (defined as surface 12) are detected using the same cost function but different smoothness constraints. The positions of surfaces 11 and 12 are used in region segmentation, where their z-axis distance-based difference is used to form a PED footprint map.

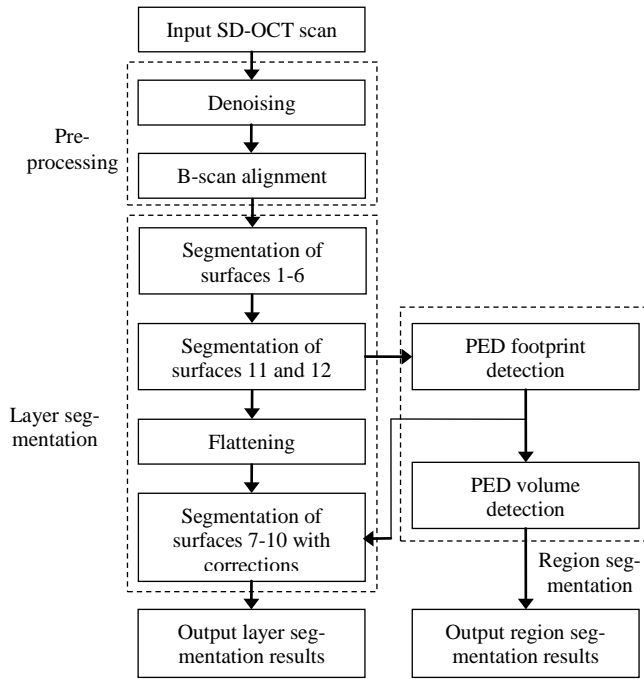


Fig. 3. Flowchart of the proposed algorithm

The 3-D PED region is also obtained. Finally, surfaces 7 and below are detected on a flattened OCT image and are corrected using the PED footprints.

The contribution of this work includes the following:

- A simple and effective alignment method is proposed that improves the performance of the 3-D graph search method while maintaining the natural curvature of retinal layers.
- The normal RPE floor, which does not exist under the PED region, is estimated using 3-D graph search method with simple constraints.
- Layers that are most dramatically affected by PED's are detected on the flattened image, where their position errors caused by intensity discontinuity can be corrected using geometric constraints.

B. Multi-resolution graph search

The 3-D graph search algorithm for optimal surface segmentation proposed by Li *et al.* [27] and its variations were successfully applied to retinal layer segmentation [1-3, 6, 7]. Boundaries between retinal layers can be modeled as terrain-like surfaces. Finding the optimal surface is transformed into computing a minimum weight closed set in a node-weighted digraph, which can be solved in polynomial time by computing a minimum s-t cut in a derived arc-weighted digraph [28-30].

Graph search for single surface detection is used in the proposed method. The volumetric image is defined as a 3-D matrix $I(x, y, z)$ with size $X \times Y \times Z$, and the surface is defined by a function $S(x, y)$, where $x \in \{0, \dots, X-1\}$, $y \in \{0, \dots, Y-1\}$, and $S(x, y) \in \{0, \dots, Z-1\}$. Two parameters, Δ_x and Δ_y , control the smoothness of feasible surfaces. More precisely, Δ_x defines the maximum of $|S(x+1, y) - S(x, y)|$

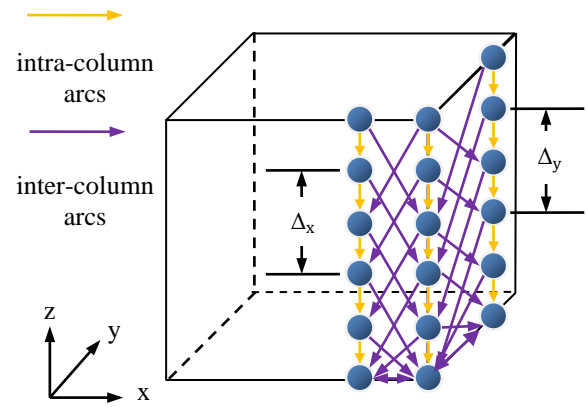


Fig. 4. Illustration of graph construction for single surface detection.

and Δ_y defines the maximum of $|S(x, y+1) - S(x, y)|$. A cost function $c(x, y, z)$ inversely related to the likelihood that the voxel belongs to the detected surface is assigned to each voxel, so that the optimal surface is the one with the minimum cost. A node-weighted directed graph $G(V, E)$ is constructed from the volumetric image. Each node in V corresponds to one and only one voxel in $I(x, y, z)$. The weight of each node is computed as

$$w(x, y, z) = \begin{cases} c(x, y, z) & \text{if } z=0 \\ c(x, y, z) - c(x, y, z-1) & \text{otherwise} \end{cases}, \quad (1)$$

so that searching for the optimal surface is transformed to seeking a minimum weight closed set. The arc set E consists of intra-column arcs and inter-column arcs. The intra-column arcs connect each node with its immediate neighbor below, and the inter-column arcs are constructed according to the smoothness constraints, as shown in Fig. 4. This graph is further transformed to an arc-weighted digraph where the optimal closed set is found by computing a minimum s-t cut. Refer to [27] for more details.

Two types of cost functions are used in the proposed method. For most layers, the basic edge-based cost function is used. By definition, surfaces 1, 3, 5, 7, 9 and 10 have the dark-to-bright transition from top to bottom of the OCT scan, while surfaces 2, 4, 6, 8 and 11 have the bright-to-dark transition. The Sobel operator is used to calculate the gradient magnitude in z-direction that forms the basic cost function. In the experiments, because the test data has low resolution in y-direction, the Sobel operator is calculated in 2-D for each B-scan (x-z plane). An additional region-based cost is calculated and added to the basic edge-based cost for detection of surface 1, to ensure that surface 1 is favored than surface 7, which also has a high-contrast dark-to-bright transition. This cost is a summation of voxel intensities in a limited region above each voxel [1]. Since the region above surface 1 is darker than that above surface 7, the voxels on surface 1 can have lower costs than those on surface 7.

Two facts are considered in determining the smoothness constraints Δ_x and Δ_y for each surface: the image resolution and the shape of surfaces. If the resolution is high, small values are used to ensure the smoothness of the surfaces. However, when the resolution is low, for certain surfaces, big difference of surface positions may exist between adjacent slices. For

example, surface 1 around the fovea and surface 11 above the PED region may have these quick changes. Therefore, for detection of these surfaces, large values of constraints are needed to ensure feasible surfaces exist. However, with large smoothness constraints, the detected surface position is more easily affected by noise or other artifacts in the OCT scan.

The multi-resolution graph search method [3] is used in our algorithm to improve the efficiency of surface detection. The 3-D OCT scan is downsampled by a factor of 2 twice in z-direction to form three resolution levels. Level 1 represents the lowest resolution and level 3 represents the highest resolution, i.e., the original data. The search for the surface in higher resolution is constrained in a subimage near the position of the surface detected in the next lower resolution. This subimage is rearranged into a rectangle so that the initial surface position lies in the center line. However, some surfaces with weak contrast may not be detectable in low resolution levels. In the proposed method, surfaces 1, 7, 11 and 12 are first detected in level 1, surfaces 2, 4 and 6 are first detected in level 2 and the remaining surfaces are detected only in level 3.

C. Pre-processing

1) Denoising by bilateral filtering

Speckle noise is the dominant quality degrading factor in OCT scans, which may affect the effectiveness and efficiency of the following image processing and analysis algorithms. Denoising methods that can effectively remove the speckles while maintaining edge-like features in the image are particularly important for segmentation tasks. Bilateral filtering [31] fulfills this requirement, which is essentially a weighted average filter, with weights that decrease with both the distance in the image plane (the spatial domain S) and the distance along the intensity axis (the range domain R). The result of bilateral filtering is given by

$$I_p^{bf} = \frac{1}{W_p^{bf}} \sum_{q \in S} G_{\sigma_s}(\|p - q\|) G_{\sigma_r}(I_p - I_q) I_q \quad (2a)$$

with $W_p^{bf} = \sum_{q \in S} G_{\sigma_s}(\|p - q\|) G_{\sigma_r}(I_p - I_q)$, (2b) where p is the pixel being processed, q is the neighboring pixel, I_p and I_q are their original intensities and I_p^{bf} is the filtering result. G_{σ_s} and G_{σ_r} are two Gaussian functions with standard deviations σ_s and σ_r , called the space and range parameters, respectively. The brute-force implementation of bilateral filtering is computationally expensive. Here we apply a fast approximation technique reported in [32]. In this scheme the bilateral filter is formulated in a higher dimension space as a convolution followed by simple nonlinear operations, and the computation can be downsampled without significantly impacting the result accuracy. The filtering is applied to each B-scan of the OCT data. The parameters are selected empirically as $\sigma_s = 20$ and $\sigma_r = 0.05$ for intensities linearly normalized to $[0, 1]$. The average processing time for each B-scan is 0.05 ± 0.0022 s. The denoising result for one B-scan is shown in Fig. 5. The noise is suppressed while the edges between layers are preserved well.

2) Alignment of B-scans

As OCT is an *in-vivo* imaging technique, eye movement is inevitable and causes distortion in the volumetric OCT data. This distortion is most notable as misalignment of the B-scans, causing the position of layers to vary greatly in consecutive

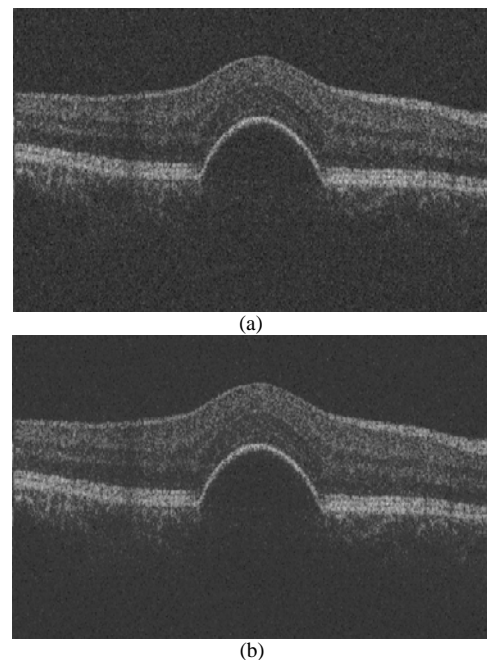


Fig. 5. Result of denoising using bilateral filtering. (a) Original B-scan (b) Denoised B-scan

B-scans and leading to difficulties for 3-D segmentation. The misalignment can be viewed in the y-z image, as in Fig. 6 (a), where each column corresponds to a B-scan. Image flattening is often employed to correct the eye movement artifacts [2, 3, 6]. However, in images with PED's, flattening may ruin the natural curvature of the edges that will be used as constraints in the subsequent segmentation, e.g., the dome like shape of the elevated RPE and the smooth surface that forms the bottom of the retina. We propose a fast method that approximately aligns the B-scans. After alignment, the smoothness of the surfaces to be detected is improved, so that they can be found by graph search with smaller smoothness constraints, and therefore are less affected by image noise, as explained in Section II.A.

The B-scan alignment works as follows. Surface 1 is first detected using the multi-resolution surface detection method, and used as a reference surface, because its edge is the most prominent among all surfaces and can be detected quite accurately even in the misaligned data. The average z position of the peripheral surface 1 in each B-scan is calculated to estimate the displacement of each B-scan. Specifically, both the left most and the right most 20% points of surface 1 are used in this calculation. Since normal fovea is naturally concave, the center part of surface 1 is excluded from the above calculation. Each B-scan is thus shifted up or down so that the average z positions of peripheral surface 1 become the same for all B-scans.

The alignment results in a smoothed appearance of all the layers in the y-z image, as shown in Fig. 6(b). The 3-D renderings of surface 1 before and after alignment are shown in Fig. 7. After alignment, the shape of surface 1 is much closer to that in the real eye.

D. Detection of surfaces 1-6

The multi-resolution graph search is then applied to the aligned data. Surfaces 1 to 6 which are not severely affected by PED's, are first detected. To achieve higher accuracy, surface 1 is detected again using the same method as in Section II.A. For

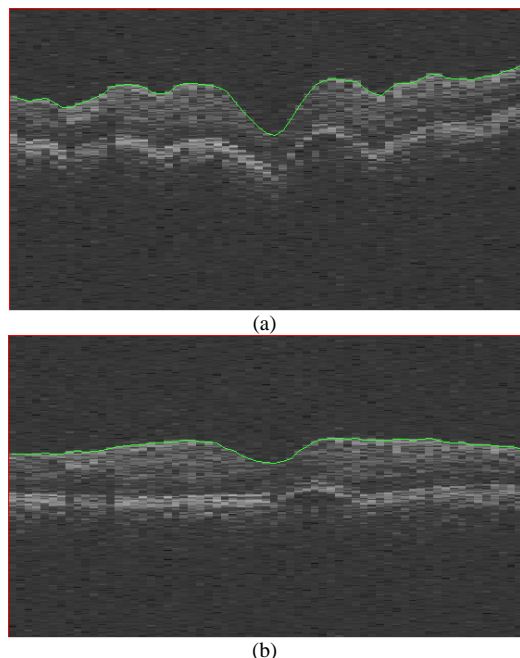


Fig. 6. The y-z image before (a) and after (b) B-scan alignment with surface 1 overlaid.

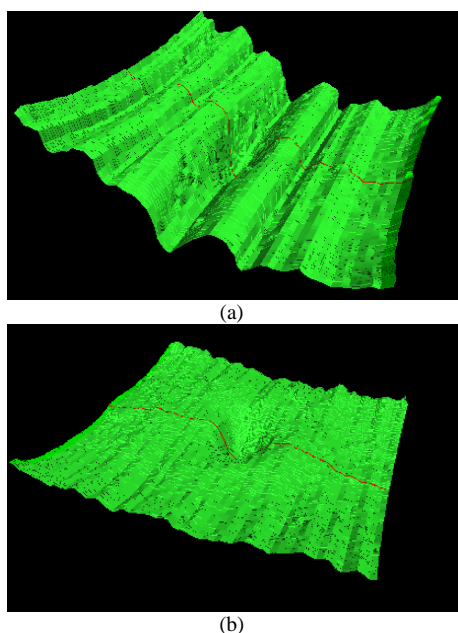


Fig. 7. Surface 1 before (a) and after (b) B-scan alignment. The red curves correspond to surface 1 in the y-z slices as shown in Fig. 6(a) and (b), respectively.

normal eyes surface 7 is detected to constrain surfaces 2-6 [3]. However, for images with PED, the CL, OSL and VM are often invisible above the detachment region, and thus cause discontinuities in surfaces 7 to 9. Nevertheless, a surface combined by 7 and 10, defined as surface 7' (see Fig. 8) can be detected, where surface 10 replaces surface 7 where it is not present. The search for this surface is constrained in the subvolume below surface 1. Similarly, surfaces 2 to 6 are detected with previously detected surface positions serving as constraints. See Table I for the order of detection, the position and smoothness constraints for each surface. Large smoothness constraints are

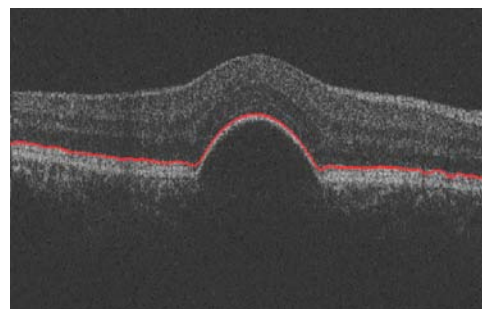


Fig. 8. Surface 7' combining surfaces 7 and 10.

TABLE I
DETAILED CONSTRAINTS AND PARAMETER SELECTION IN SURFACE DETECTION.
NOTE THAT $\Delta_x = 1$ FOR ALL SURFACES AND ALL LEVELS.

Order in detection	Surface #	Surface above	Surface below	Initial Detection level	Δ_y in Initial level
1	1	N/A	N/A	1	6
2	7'	1	N/A	1	6
3	2	1	7	2	3
4	4	2	7	2	3
5	6	4	7	2	3
6	3	2	4	3	6
7	5	4	6	3	6
8	11	7'	N/A	1	6
9	12	7'	N/A	1	1
10	10	7	11	3	1
11	8	7	10	3	1
12	9	8	10	3	1

set in y direction for surfaces 1 and 7' at resolution level 1 to allow quick changes of surface positions in adjacent B-scans caused by the fovea or the PED. To further remove the influence of noise, each surface is smoothed in the x direction using a moving average filter.

E. Detection of the abnormal region

To correct the discontinuities in surfaces 7-9 caused by PED, the location of PED needs to be estimated. This is done by detecting the elevated RPE floor (surface 11) and the normal RPE floor (surface 12), and then finding their differences. Size and mean intensity values are also considered to remove false positives.

1) Detection of the elevated RPE floor and the estimated normal RPE floor

Surfaces 11 and 12 are detected in the subvolume below surface 7'. The real RPE floor changes abruptly and becomes dome-shaped in the PED region while its original pre-disease position used to form a smooth surface. Therefore, with the same bright-to-dark edge-related cost function, surface 11 can be detected by employing a large smoothness constraint and surface 12 can be detected by employing a small smoothness constraint. Even if no edge appears under the PED dome shape, this parameter constrains surface 12 to follow the smooth bottom of the retina. However, due to the loose constraint, surface 11 may not follow the bottom of the retina properly in areas outside PED's, but may be distracted by the choroid. Therefore we correct surface 11 by replacing it with surface 12 wherever it goes below surface 12. See Fig. 9 for the detected surfaces 11 and 12.

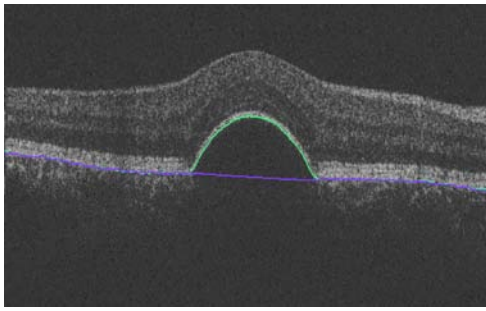


Fig. 9. Detected surfaces 11 and 12.

2) PED footprints and volume detection

The PED footprints are generated in the x-y plane indicating which A-scans are associated with PED's. First, a rough set of (x,y) coordinates are obtained where surface 11 is more than d_1 pixels higher than surface 12. Then these points are grouped into connected components, and regions with area less than a threshold A are excluded as false positives. In the next step, to make the boundaries more accurate, these footprints are extended via hysteresis thresholding to include connected points where surface 11 is more than d_2 ($d_2 < d_1$) pixels higher than surface 12. Subsequently the 3-D PED volumes are detected as the set of voxels between surfaces 11 and 12 within each footprint. Finally, the mean intensity of each PED volume is used to reject false positives, owing to the fact that serous PED's usually appear as dark regions in OCT. PED volumes with normalized mean intensity less than a threshold T are discarded as false positive. Examples of the initial PED footprint detection result and final footprint after edge refinement and rejection of false positives are shown in Fig. 10(a) and (b), respectively. The details of parameter selection is described in Section IV.A.

F. Detection of surfaces 7-10

In OCT scans for normal eyes, surfaces 7-10 are relatively flat surfaces with reasonably uniform distances between adjacent ones. If the fluid-filled volume of PED is removed, these geometric constraints can be approximately restored. This is achieved by flattening of the OCT volume using surface 11 detected in Section II.E as the reference surface. Thus the invisible portions of surfaces 7-9 can be estimated in the flattened image.

Flattening refers to shifting the A-scans up or down so that surface 11 becomes a flat surface. Surface 7' detected in Section II.D is also shifted with the data. In each B-scan, surface 7' inside the PED footprint is corrected by second-order polynomial curve interpolation. After the correction, surface 7 is used to constrain surfaces 8 to 10, which is detected using small smoothness constraints, as shown in Table I. Surfaces 8 and 9 are also corrected by interpolation within the PED footprint. In the end, these surfaces are converted back to their positions in the original OCT volume. See Fig. 11 for the flattened image and the results for surfaces 7 to 10.

III. EXPERIMENTAL METHODS

Macula-centered SD-OCT scans of 20 eyes from 20 subjects diagnosed with serous PED's and 20 normal eyes from 20 subjects (the controls) were acquired using Topcon 3D-OCT

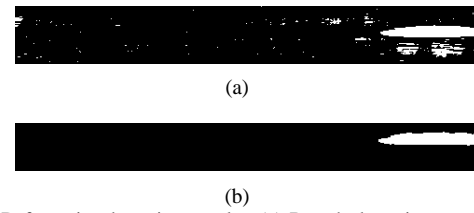


Fig. 10. PED footprint detection results. (a) Rough detection result from difference between surface 11 and 12. (b) PED footprint after edge refinement and rejection of false positives.

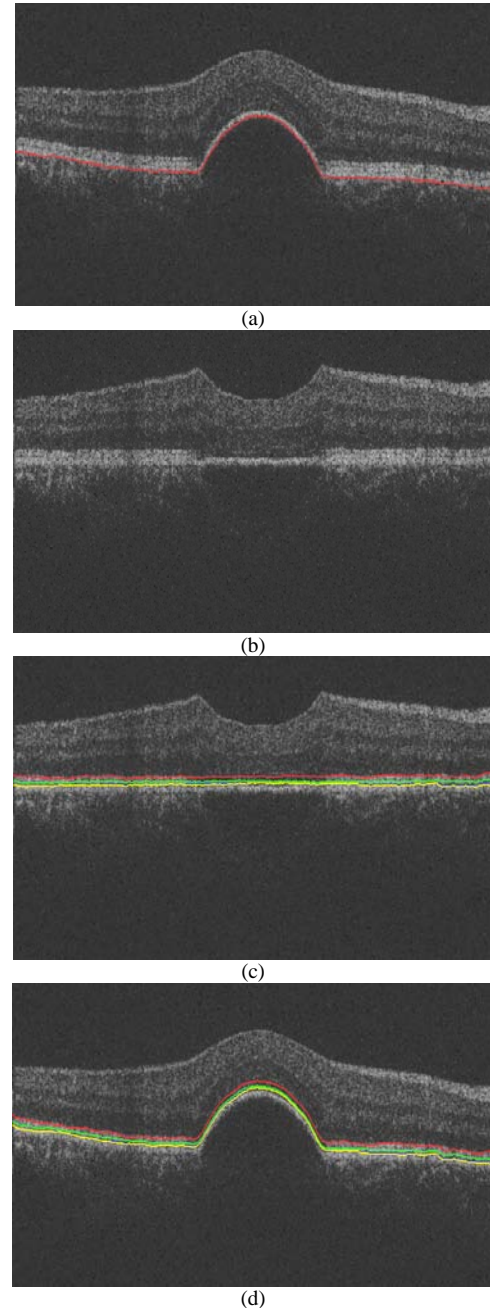


Fig. 11. Detection of surfaces 7-10 on a flattened image. (a) Original B-scan with reference surface overlaid, (b) Flattened B-scan, (c) Surfaces 7-10 overlaid on flattened image, surface 7 is shown in red, surface 8 in green, surface 9 in blue and surface 10 in yellow. Surface 9 may not be visible because it overlaps with surface 10 in many places, (d) Surfaces 7-10 mapped back to the original image.

1000 (Topcon Corporation, Tokyo, Japan). OCT image stacks

comprised of $512 \times 64 \times 480$ voxels with voxel size of $11.72 \times 93.75 \times 3.50 \mu\text{m}^3$. This study was approved by the Intuitional review board of Joint Shantou International Eye Center and adhered to the tenets of the Declaration of Helsinki. Because of its retrospective nature, informed consent was not required from subjects.

To evaluate the layer segmentation results, two retinal specialists manually traced the surfaces in the B-scan images independently to form the ground truth. Due to the time consumption of manual segmentation, for each 3-D OCT volume, only 10 out of the 64 B-scans, which were uniformly distributed in the volumetric data, were traced. Among the 200 manually traced B-scans from the PED dataset, PED's were present in 50 B-scans, according to the ground truth of region segmentation. The average of the two tracings defined the reference standard. Surfaces 3, 8 and 9 were excluded because they were not always discernible to human eyes on the available data sets. Surface 12 was also excluded since it was only a virtual structure used for reference. The unsigned border positioning errors were calculated for each surface by measuring absolute Euclidean distances in the z-axis between segmentation results of the proposed algorithm and the reference standard. The unsigned border positioning errors were compared with the unsigned border positioning differences between the two manual tracings and also compared with results obtained by the general Iowa Reference Algorithm [14] not specifically designed to handle PED's. Paired t-tests were used to compare the segmentation errors and a p -value less than 0.05 was considered statistically significant.

To evaluate the PED volume segmentation results, one retinal specialist manually segmented the PED regions in all B-scans to form the ground truth. The accuracy in terms of true positive volume fraction (TPVF), false positive volume fraction (FPVF) and positive predicative value (PPV) were calculated as follows [33]:

$$\text{TPVF} = \frac{|C_{\text{TP}}|}{|C_{\text{GT}}|}, \quad (3a)$$

$$\text{FPVF} = \frac{|C_{\text{FP}}|}{|V| - |C_{\text{GT}}|}, \quad (3b)$$

$$\text{PPV} = \frac{|C_{\text{TP}}|}{|C_{\text{TP}}| + |C_{\text{FP}}|}, \quad (3c)$$

where $|\cdot|$ denotes volume, C_{TP} denotes the true positive set, C_{FP} denotes the false positive set, C_{GT} denotes the set of voxels defined as PED volume in ground truth, and V denotes the total volume of the retina, which is defined as the volume between surfaces 1 and 12 detected by the proposed algorithm.

IV. RESULTS

A. Parameter selection

For surface detection, the smoothness constraints are selected according to the rules described in Section II.A and listed in Table I. For the tested data, the resolution is much higher in the x direction than the y direction. Therefore Δ_x is set to 1 for all surfaces and Δ_y varies for different surfaces in the initial detection level. As surfaces 1, 7' and 11 are the ones most affected by the shape of the fovea or the PED's, large Δ_y is required, which is set as $\Delta_y = 6$ at resolution level 1. Larger values are also acceptable since these surfaces have strong contrast and are minimally affected by image noise. Surfaces

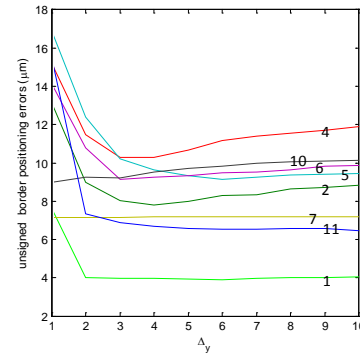


Fig. 12. Surface segmentation errors with different smoothness constraints in y-direction. The surface number/label is indicated on each curve.

2-6 can be affected by the fovea or the PED to some extent, have weaker contrast and are more easily affected by noise. Therefore medium Δ_y is set for these surfaces, with $\Delta_y = 3$ at resolution level 2, and $\Delta_y = 6$ at resolution level 3. Surface 12 and surfaces 8-10 on the flattened image are required to be smooth surfaces. Therefore small Δ_y is needed, which is set as $\Delta_y = 1$. For the refining step in multi-resolution surface detection, the surfaces are detected on a reshaped image where the initial position lies in the center. Assuming the initial detection is accurate enough, the surface position in higher resolution will be close to the center line. Therefore, only small smoothness constraints ($\Delta_x = \Delta_y = 1$ in experiments) are needed.

To verify the validity of the choice of Δ_y , segmentation results are obtained on the PED dataset with Δ_y in the initial detection level ranging from 1 to 10 for all surfaces excluding surfaces 3, 8 and 9. Note that the results are obtained by changing Δ_y for one surface at a time, while the rest parameters are fixed with the values in Table I. Hence only the influence of Δ_y on the current surface is analyzed, and the possible error propagation between surfaces is not considered. The unsigned border positioning errors are calculated and plotted in Fig. 12. As shown in the figure, for surfaces 1, 2, 4, 5, 6 and 11, the errors are large when Δ_y is too small, showing the incapability in capturing surface changes. The errors decrease first with the increase of Δ_y , and after reaching the minimum, they only increase slightly with the increase of Δ_y . For surfaces 1 and 11 with high contrast, the results are especially insensitive to the increase of Δ_y . This confirms the effect of noise when large smoothness constraints are applied. The error of surface 7 is almost constant because the influence of Δ_y is reduced by the correction step. The error of surface 10 increases slightly with the increase of Δ_y , because it is detected on the flattened image.

For PED footprint and volume detection, the distance thresholds d_1 , d_2 and the area threshold A are selected empirically. However, as tested, the region segmentation performance is not sensitive to perturbations of these parameters. Empirically determined, the suggested ranges of parameters are: $d_1 = 3 \sim 7$, $d_2 = 1 \sim 2$, and $A = 30 \sim 70$ in pixels. For different combinations of parameters inside these ranges, the variations of TPVF and PPV are both less than 1% and the variation of FPVF is less than 0.01%. For robustness, small values are preferred so that PED regions with minor elevation of RPE and small sizes

would not be missed. Even if some false positives caused by noise would be included after this step, most of them will be ruled out by the intensity criteria in place. As a result, low false positive ratios will still be obtained. For the reported results in Section IV.D, $d_1 = 3$, $d_2 = 1$, and $A = 30$ were used. The intensity threshold T is set as the adaptive Otsu threshold [34] since the OCT scans have a double-peak histogram.

B. Layer segmentation results for the PED dataset

Examples of layer segmentation results are shown in Fig. 13 in both 2-D and 3-D. The visualization software OCTExplorer contained in the Iowa Reference Algorithms [14] is used to show the segmentation results (including the previous figures).

The mean and standard deviation of unsigned border positioning errors for each surface, computed on all manually traced B-scans from the PED dataset, are shown in Table II, and compared with inter-observer variability and the errors resulting from employing the Iowa Reference Algorithm [14]. The p -values are shown in Table III, where bold numbers indicate that the proposed method has statistically significantly better performance. Compared with the unsigned difference between observers, the unsigned positioning errors of surfaces 1 and 11 are significantly smaller, the unsigned positioning errors of surfaces 4 and 10 are significantly bigger, and the unsigned positioning errors of surfaces 2, 5, 6 and 7 are statistically indistinguishable from the unsigned difference between observers. The overall mean unsigned error is $7.87 \pm 3.38 \mu\text{m}$, which is statistically indistinguishable from the mean unsigned difference between two observers ($7.80 \pm 2.54 \mu\text{m}$). Compared with [14], the unsigned positioning errors of surfaces 2 and 11 are statistically significantly smaller, the unsigned positioning errors of the other surfaces are statistically indistinguishable, and the overall mean unsigned error is statistically significantly smaller.

The results in Table II only show minor improvement over [14] because the PED is a local structure. Only a small proportion of the layers exhibits dramatic morphological changes, and the segmentation method for normal retinas performed well in other places. To better evaluate the layer segmentation performance near the PED region, the mean and standard deviation of unsigned border positioning errors calculated only on the 50 B-scans with PED's, are shown in Table IV, and compared with both inter-observer variability and the errors resulting from employing the Iowa Reference Algorithm [14]. The p -values are shown in Table V, where bold numbers indicate that the proposed method has statistically significantly better performance. The unsigned positioning error of surface 1 is significantly smaller than the inter-observer differences. Errors of the other surfaces and the overall error are statistically indistinguishable from the unsigned difference between observers. Compared with [14], except that the error of surface 1 is statistically indistinguishable, errors of all the other surfaces are significantly smaller, and the overall mean unsigned error is significantly smaller. This proves that the proposed algorithm outperforms the algorithm [14] in segmenting abnormal retinal layers.

The mean and standard deviation of signed border positioning errors for each surface are shown in Table VI. For most surfaces, the mean signed errors are negative, indicating that

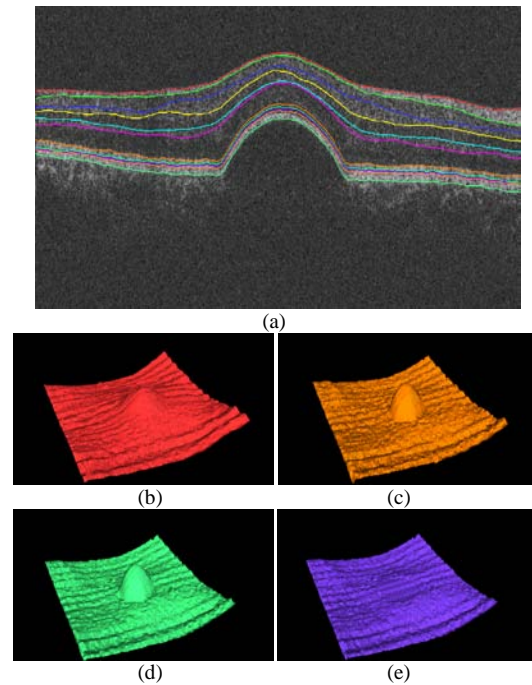


Fig. 13. Layer segmentation results. (a) 12 surfaces overlaid on B-scan. (b)-(e) 3-D visualization of surfaces 1, 7, 11 and 12.

TABLE II
SUMMARY OF MEAN UNSIGNED BORDER POSITIONING ERRORS[†] FOR ALL LABELED B-SCANS OF PED DATA

Surface	Algo. vs. Ref.	Obs. 1 vs. Obs. 2	[14] vs. Ref
1	3.91±0.65	5.28±0.79	4.07±0.67
2	7.79±2.47	7.22±1.33	9.82±2.55
4	10.30±2.57	8.09±2.08	12.78±7.36
5	9.14±3.83	9.48±4.59	12.36±8.81
6	9.14±2.87	8.66±1.61	11.42±8.25
7	7.19±3.57	7.18±1.73	8.36±4.26
10	8.99±3.42	7.37±2.39	10.16±5.87
11	6.53±2.28	9.09±1.36	9.49±5.38
Overall	7.87±3.36	7.81±2.56	9.81±6.42

[†]Mean ± SD in μm , $3.5\mu\text{m} = 1 \text{ pixel}$.

TABLE III
SUMMARY OF p -VALUES OF MEAN UNSIGNED BORDER POSITIONING ERRORS FOR ALL LABELED B-SCANS OF PED DATA[†]

Surface	p value Algo. vs. Ref.	p value Algo. vs. [14]
1	<<0.001	0.2888
2	0.2951	<<0.001
4	0.0009	0.0846
5	0.6493	0.0742
6	0.2914	0.1574
7	0.9896	0.2048
10	0.0398	0.3036
11	<<0.001	0.0030
Overall	0.7357	<<0.001

[†]Numbers in bold indicate statistically significantly better performance.

the automated segmentation is located slightly above the surfaces obtained by manual tracing. This is caused by the difference in perceived edge and the position of maximum gradient magnitude.

The best and worst performance cases are shown in Fig. 14 and Fig. 15, respectively (surfaces 3, 8, 9 and 12 are omitted). In Fig. 14, the PED region is small, the retina is almost normal and the image quality is good. However, in Fig. 15 the PED

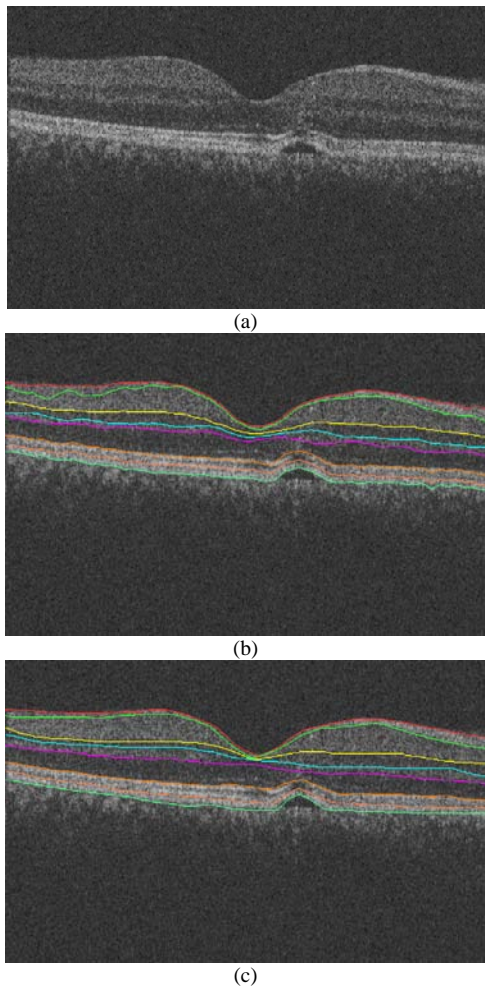


Fig. 14. Segmentation results of 8 segmented surfaces in the best performance case. (a) Original B-scan (b) Segmentation results overlaid on original B-scan. (c) Manual segmentation (average of the two tracings).

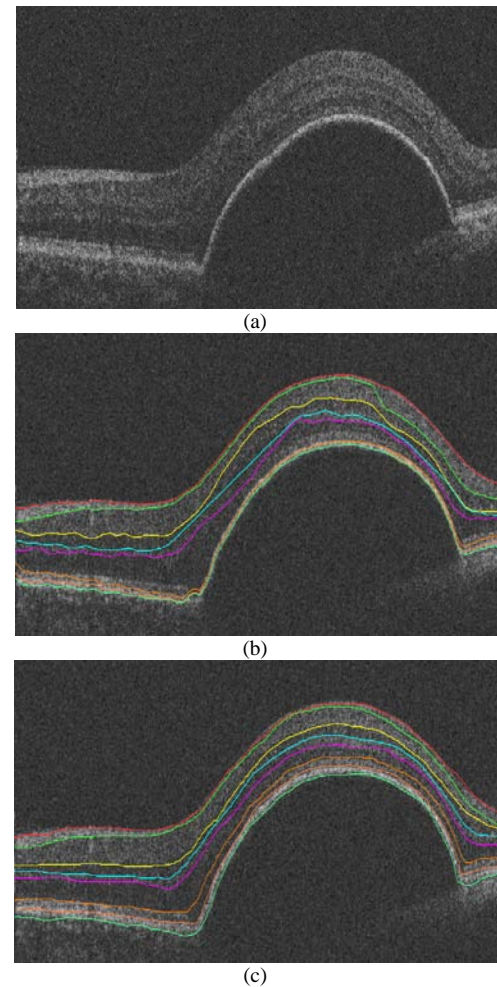


Fig. 15. Segmentation results of 8 segmented surfaces in the worst performance case. (a) Original B-scan (b) Segmentation results overlaid on original B-scan. (c) Manual segmentation (average of the two tracings).

TABLE IV

SUMMARY OF MEAN UNSIGNED BORDER POSITIONING ERRORS[†] FOR B-SCANS WITH PED

Surface	Algo. vs. Ref.	Obs. 1 vs. Obs. 2	[14] vs. Ref
1	4.21±0.89	5.52±1.53	5.17±1.56
2	8.65±3.76	7.07±1.62	10.90±3.36
4	11.48±3.09	8.90±3.02	15.70±6.90
5	11.81±4.30	11.87±6.20	16.08±8.45
6	13.00±4.54	10.25±2.79	16.68±9.55
7	8.70±2.99	10.54±3.66	14.17±5.55
10	9.70±2.95	8.82±3.99	17.99±7.88
11	8.59±6.52	9.41±2.41	18.55±7.60
Overall	9.52± 4.61	9.05± 3.86	14.41±7.87

[†]Mean ± SD in μm , $3.5\mu\text{m} = 1 \text{ pixel}$.

occupies a large portion of the scanned area. The boundaries between layers are unclear, especially above the PED. Even with correction, the algorithm fails to retrieve the correct position of surface 7 above PED. Therefore, poor image quality, probably caused by severe retinal abnormalities, can affect the performance of the proposed algorithm.

C. Layer segmentation results for the normal dataset

Although the proposed method is designed for retinas with serous PED's, the method can be directly applied to segmentation of normal retinas. In this case, surfaces 11 and 12 will

TABLE V

SUMMARY OF *p*-VALUES OF MEAN UNSIGNED BORDER POSITIONING ERRORS FOR B-SCANS WITH PED[†].

Surface	<i>p</i> value Algo. vs. Ref.	<i>p</i> value Algo.vs. [14]
1	<<0.001	0.4765
2	0.0733	<<0.001
4	0.0062	<<0.001
5	0.9503	0.0430
6	0.0056	0.0132
7	0.0981	0.0140
10	0.2834	<<0.001
11	0.5595	<<0.001
Overall	0.1806	<<0.001

[†]Numbers in bold indicate statistically significantly better performance.

TABLE VI

SUMMARY OF MEAN SIGNED BORDER POSITIONING ERRORS[†]

Sur-face	PED data		Normal data	
	Algo. vs. Ref.	Obs. 1 vs. Obs. 2	Algo. vs. Ref.	Obs. 1 vs. Obs. 2
1	1.30±1.09	- 0.88±1.30	- 0.18±0.62	- 0.50±0.78
2	- 3.08± 3.36	1.40±2.45	- 5.03±1.75	- 0.44±0.99
4	- 6.54±3.67	- 1.40±3.85	- 7.23±1.75	4.65±1.96
5	- 0.38±4.76	- 3.08±6.65	0.66±0.95	- 4.32±1.99
6	- 2.21±3.11	- 1.30±3.22	- 3.19±1.68	0.52±2.30
7	3.39±4.03	1.05±3.08	- 0.36±0.57	- 0.74±1.31
10	- 2.66±7.39	1.40±4.09	- 5.89±4.31	- 4.62±3.09
11	- 3.29±3.01	3.64±3.89	- 3.68±1.35	0.54±2.24
Overall	- 1.68±4.97	0.11±4.27	- 3.11±3.33	- 0.61±3.36

[†]Mean ± SD in μm , $3.5\mu\text{m} = 1 \text{ pixel}$.

represent the same surface and their detection results will overlap in most places. Even if surface 11 has more fluctuation due to the impact of noise, as it is obtained with a large smoothness constraint, the regions between surfaces 11 and 12 will be excluded as false positives in PED detection. Then flattening with respect to surface 11 is just the same as was established in [2, 3, 6], which further removes the eye movement artifacts. Additionally, the correction of surfaces 7-9 will be automatically skipped when no PED region is detected.

To test the method's performance for normal data, we applied the proposed method to OCT images from a control group of 20 normal subjects. The mean and standard deviation of unsigned border positioning errors for each surface are shown in Table VII and compared with inter-observer variability and the errors resulting from employing the Iowa Reference Algorithm [14]. The p -values are shown in Table VIII, where bold numbers indicate that the proposed method has statistically significantly better performance. The overall mean unsigned error of the proposed algorithm is significantly smaller than the mean unsigned difference between two observers. Compared with [14], the overall error mean unsigned error is statistically indistinguishable. This proves that the proposed algorithm maintains its good performance for normal retinas.

D. Results of PED volume segmentation

An example of PED volume segmentation result is shown in Fig. 16. As serous PED is one case of symptomatic exudate-associated derangement (SEAD) discussed in [20], the results of the proposed method are compared with those obtained by the GS-GC algorithm [20] on the same dataset. In implementation of the GS-GC algorithm, to avoid detection of other SEAD regions, surfaces 11 and 12 are used as the two constraining surfaces. The TPVF, FPVF and PPV of both methods with p values are shown in Table IX. The proposed algorithm achieves statistically comparable results with the GS-GC algorithm in all three measures. However, the GS-GC algorithm is a supervised method which requires training, and both the initialization step using classification and the following graph-based segmentation step is time consuming. The proposed method is unsupervised and less computationally expensive, as will be shown in Section IV.E.

In some case with minor elevation of the RPE (see Fig. 17), surface 12 may follow the elevated RPE floor instead of the bottom of RPE, causing false negative detection and thus bringing down the TPVF. The FPVF of the proposed method is low owing to three facts. Firstly the PED volume is relatively small comparing to the total retina volume. Secondly the proposed method confines PED detection between the detected surfaces 11 and 12, thus reducing the chance of false positives. Finally, the false positive removal step using size and intensity is effective. The PPV further indicates the proportion of true positives among all detected regions.

The PED volume segmentation was also tested on the normal data. A perfect FPVF = 0 was achieved, indicating that the algorithm is highly effective in distinguishing normal retinas from those with PED's.

E. Computational time

The proposed algorithm is implemented in C++ and tested on a PC with Intel i7-3770 CPU@3.40GHz and 16GB of RAM,

TABLE VII
SUMMARY OF MEAN UNSIGNED BORDER POSITIONING ERRORS[†] FOR NORMAL DATA

Surface	Algo. vs. Ref.	Obs. 1 vs. Obs. 2	[14] vs. Ref
1	2.92±0.23	4.33±0.38	3.30±0.27
2	7.29±1.04	5.34±0.57	7.43±0.70
4	8.43±1.17	7.78±1.11	9.02±1.09
5	4.62±0.68	7.43±1.32	5.81±0.89
6	6.08±1.25	7.07±0.90	5.67±0.84
7	2.53±0.25	4.06±0.77	3.97±0.42
10	7.21±3.57	7.75±3.60	4.88±1.96
11	5.39±0.89	7.66±1.59	4.79±0.81
Overall	5.56± 2.47	9.05± 3.86	5.61±2.00

[†]Mean ± SD in μm , $3.5\mu\text{m} = 1 \text{ pixel}$.

TABLE VIII
SUMMARY OF p -VALUES OF MEAN UNSIGNED BORDER POSITIONING ERRORS FOR NORMAL DATA[†].

Surface	p value Algo. vs. Ref.	p value Algo. vs. [14]
1	<< 0.001	<< 0.001
2	<<0.001	0.5354
4	0.0589	0.0054
5	<< 0.001	<< 0.001
6	<< 0.001	0.0274
7	<< 0.001	<< 0.001
10	0.4430	0.0049
11	<< 0.001	<<0.001
Overall	<< 0.001	0.7067

[†]Numbers in bold indicate statistically significantly better performance.

TABLE IX
PED VOLUME SEGMENTATION RESULTS, COMPARED WITH THE GS-GC ALGORITHM [20]

	Proposed Algo.	GS-GC Algo.[20]	p value
TPVF	87.1%±21.7%	84.1%±21.7%	0.6706
FPVF	0.37%±0.54%	0.44%±0.78%	0.6252
PPV	81.2%±20.2%	81.2%±25.7%	0.9675

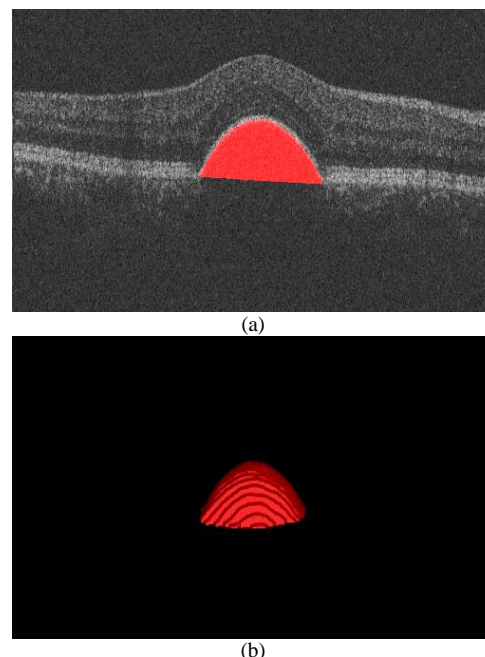


Fig. 16. PED volume segmentation results. (a) Detected PED volume overlaid on B-scan (b) 3-D visualization of the detected PED volume.

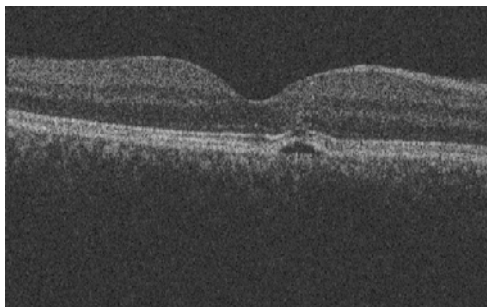


Fig. 17. False negative case of PED volume detection.

where only single core is utilized. The average running time of the algorithm is 220 ± 51 s. The preprocessing step takes 15 ± 5 s in average. The detection of surface 12 is the most time consuming, which takes about 150 ± 32 s in average, because the discontinuity of edge below the PED region adds to the difficulty of finding the optimal surface. For comparison, the Iowa reference algorithm for layer segmentation requires 62 ± 12 s and the GS-GC algorithm for region segmentation requires 456 ± 103 s.

V. CONCLUSIONS AND DISCUSSION

We proposed an unsupervised method for automated segmentation of retinal layers on SD-OCT scans of eyes with serous PED. After denoising using fast bilateral filtering, the B-scans are aligned using the upper boundary of the retina. This alignment improves the smoothness of the surfaces to be detected and enhances the accuracy of the segmentation. Then the surfaces defining the boundaries between consecutive layers are detected based on multi-resolution single surface graph search. Surfaces 1 to 6, and a surface combined by surfaces 7 and 10 are detected on the denoised and aligned data. Then surfaces 11 and 12 corresponding to the elevated RPE and the estimated normal RPE floor are also detected, whose difference is used to find the PED footprints. Surface 11 is used as the reference surface for flattening of the retina. Then surface 7 is corrected based on its smoothness on the flattened image. Surfaces 8-10 are also detected on the flattened image with necessary corrections.

For the tested PED dataset, the overall layer segmentation errors are statistically indistinguishable from the inter-observer variability, and statistically significantly smaller than errors obtained from employing the general Iowa Reference Algorithm [14]. Though the proposed algorithm is designed for retinas with serous PED's, it also works well for normal retinas. For the tested normal dataset, the overall layer segmentation errors are statistically smaller than the inter-observer difference, and statistically indistinguishable from errors obtained from employing the Iowa Reference Algorithm [14]. Although the method is not the most efficient for normal retina segmentation, it represents a major advancement of the field allowing segmentation of the retinal layers in both normal and diseased retinal images, thus bypassing a need for disease-specific diagnosis prior to retinal analysis.

Simultaneous detection and segmentation of the PED volume is also achieved. The PED volume segmentation is of high true positive ratio and low false positive ratio, which is statistically comparable to the results obtained by the GS-GC me-

thod [20].

The proposed algorithm is 3-D, but some of the calculations, including denoising, gradient calculation for cost function and smoothing of the detected surfaces, are constrained in 2-D B-scans. This allows big difference in adjacent B-scans caused by low resolution in the y direction of the available data. For OCT data with higher resolution in the y direction, their 3-D counterparts should be used to fully utilize the contextual information.

The proposed algorithm can be extended to other pathological cases where RPE deformation occurs. It provides a means to remove the sub-RPE fluid region and to approximately restore the original shape of the retinal layers. This method can be extended to other pathological cases where intraretinal or sub-retinal fluids are present. In the future, we will consider detection of these regions and using the information to improve the layer segmentation results.

In summary, as an accurate and efficient replacement of manual segmentation, the proposed algorithm can be utilized for quantitative analysis of features of individual retinal layers for both eyes with serous PED's and normal eyes. The algorithm also detects the PED volume, providing its size, shape and position information. With the current efficiency, the reported work can be used in off-line clinical or pathology studies. However, with further optimization in implementation, additional speed-up will be accomplished and the reported approach will become suitable for clinical practice.

REFERENCES

- [1] M. K. Garvin, M. D. Abramoff, R. Kardon, S. R. Russell, X. Wu, and M. Sonka, "Intraretinal layer segmentation of macular optical coherence tomography images using optimal 3-D graph search", *IEEE Trans. Med. Imag.*, Vol. 27, No. 10, pp. 1495-1505, Oct. 2008.
- [2] M. K. Garvin, M. D. Abramoff, X. Wu, S. R. Russell, T. L. Burns, and M. Sonka, "Automated 3-D intraretinal layer segmentation of macular spectral-domain optical coherence tomography images", *IEEE Trans. Med. Imag.*, Vol. 28, No. 9, pp. 1436-1447, Sept. 2009.
- [3] K. Lee, "Segmentations of the intraretinal surfaces, optic disc and retinal blood vessels in 3D-OCT scans." Ph.D. dissertation, University of Iowa, 2009.
- [4] S. Lu, C. Y. Cheung, J. Liu, J. H. Lim, C. K. Leung, and T. Y. Wong, "Automated layer segmentation of optical coherence tomography images", *IEEE Trans. Biomed. Eng.*, Vol. 57, No. 10, pp. 2605-2608, Oct. 2010.
- [5] A. Yazdanpanah, G. Hamarneh, B. R. Smith, and M. V. Sarunic, "Segmentation of intra-retinal layers from optical coherence tomography images using an active contour approach", *IEEE Trans. Med. Imag.*, Vol. 30, No. 2, pp. 484-496, Feb. 2011.
- [6] Q. Song, J. Bai, M. K. Garvin, M. Sonka, J. M. Buatti, and X. Wu, "Optimal multiple surface segmentation with shape and context priors", *IEEE Trans. Med. Imag.*, Vol. 32, No. 2, pp. 376-386, Feb. 2013.
- [7] P. A. Dufour, L. Ceklic, H. Abdillahi, S. Schröder, S. De Dzanet, U. Wolf-Schnurrbusch, and J. Kowal, "Graph-based multi-surface segmentation of OCT data using trained hard and soft constraints", *IEEE Trans. Med. Imag.*, Vol. 32, No. 3, pp. 531-543, Mar. 2013.
- [8] Q. Yang, C. A. Reisman, Z. Wang, Y. Fukuma, M. Hangai, N. Yoshimura, A. Tomidokoro, M. Araie, A. S. Raza, D. C. Hood, and K. Chan, "Automated layer segmentation of macular OCT images using dual-scale gradient information", *Opt. Express*, Vol. 18, pp. 21 293-307, 2010.
- [9] S. J. Chiu, X. T. Li, P. Nicholas, C. A. Toth, J. A. Izatt, S. Farsiu, "Automatic segmentation of seven retinal layers in SDOCT images congruent with expert manual segmentation". *Opt. Express*, Vol. 18, No.18, pp.19413-28, 2010.
- [10] J. Novosel, K. A. Vermeer, G. Thepass, H. G. Lemij, and L. J. van Vliet, "Loosely coupled level sets for retinal layer segmentation in optical coherence tomography," in *proc. IEEE ISBI*, pp 1010-1013, 2013

- [11] K. A. Vermeer, J. van der Schoot, H. G. Lemij, and J. F. de Boer, "Automated segmentation by pixel classification of retinal layers in ophthalmic OCT images," *Biomed. Opt. Express*, Vol. 2, pp. 1743–56, 2011.
- [12] R. Kafieh, H. Rabbani, M. D. Abramoff, and M. Sonka, "Intra-retinal layer segmentation of 3D optical coherence tomography using coarse grained diffusion map," *Med. Image Anal.*, Vol. 17, pp. 907–928, 2013.
- [13] A. Lang, A. Carass, M. Hauser, E. S. Sotirchos, P. A. Calabresi, H. S. Ying, and J. L. Prince, "Retinal layer segmentation of macular OCT images using boundary classification," *Biomed. Opt. Express*, Vol. 4, pp. 1133–52, 2013.
- [14] The Iowa Reference Algorithms (Iowa Institute for Biomedical Imaging, Iowa City, IA.) [Online]. <http://www.biomed-imaging.uiowa.edu/downloads/>
- [15] X. Chen, P. Hou, C. Jin, W. Zhu, X. Luo, F. Shi, M. Sonka and H. Chen, "Quantitative analysis of retinal layers' optical intensities on 3D optical coherence tomography," *Invest. Ophthalmol. Vis. Sci.*, vol. 54, No. 10, pp. 6846-6851, Oct, 2013.
- [16] K. Lee, M. Niemeijer, M. K. Garvin, Y. H. Kwon, M. Sonka, and M. D. Abràmoff, "Segmentation of the optic disc in 3-D OCT Scans of the optic nerve head", *IEEE Trans. Med. Imag.*, Vol. 29, No. 1, pp. 159-168, Jan. 2010.
- [17] F. M. Penha, P. J. Rosenfeld, G. Gregori, M. Falcão, Z. Yehoshua, F. Wang, and W. J. Feuer, "Quantitative imaging of retinal pigment epithelial detachments using spectral-domain optical coherence tomography", *Am J Ophthalmol.*, Vol. 153, No.3, pp. 515-523, Mar, 2012.
- [18] G. Gregori, F. Wang, P. J. Rosenfeld, "Spectral domain optical coherence tomography imaging of drusen in nonexudative age-related macular degeneration", *Ophthalmol.*, Vol. 118, No.7, pp. 1373–1379, Mar. 2011.
- [19] W. Ding, M. Young, S. Bourgault, S. Lee, D. A. Albiani, A. W. Kirker, F. Forooghian, M. V. Sarunic, A. B. Merkur, and M. F. Beg, "Automatic detection of subretinal fluid and sub-retinal pigment epithelium fluid in optical coherence tomography images", in *Proc. Int. Conf. IEEE EMBS*, Osaka, Japan, pp.1388-1391, July 2013.
- [20] X. Chen, M. Niemeijer, L. Zhang, K. Lee, M. D. Abràmoff, and M. Sonka, "Three-dimensional segmentation of fluid-associated abnormalities in retinal OCT: probability constrained graph-search-graph-cut", *IEEE Trans. Med. Imag.*, Vol. 31, No. 8, pp. 1521-1531, Aug. 2012.
- [21] P. A. Dufour, H. Abdillahi, L. Ceklic, U. Wolf- Schnurrbusch, and J. Kowal, "Pathology hinting as the combination of automatic segmentation with a statistical shape model", in *Proc. MICCAI*, Nice, France, pp. 599-606, Oct. 2012.
- [22] G. Quellec, K. Lee, M. Dolejsi, M. K. Garvin, M. D. Abràmoff, and M. Sonka, "Three-dimensional analysis of retinal layer texture: Identification of fluid-filled regions in SD-OCT of the macula," *IEEE Trans. Med. Imag.*, Vol. 29, No. 6, pp. 1321–1330, Jun. 2010.
- [23] X. Chen, L. Zhang, E. H. Sohn, K. Lee, M. Niemeijer, J. Chen, M. Sonka and M. D. Abràmoff, "Quantification of external limiting membrane disruption caused by diabetic macular edema from SD-OCT", *Invest. Ophthalmol. Vis. Sci.*, Vol. 53, No. 13, pp.8042-8048, Dec. 2012.
- [24] S. Mrejen, D. Sarraf , S.K.Mukkamala, and K.B.Freund, "Multimodal imaging of pigment epithelial detachment: a guide to evaluation", *Retina*, Vol. 33 No. 9, pp.1735-1762, Oct. 2013.
- [25] S. Zayit-Soudry, I. Moroz, and A. Loewenstein, "Retinal pigment epithelial detachment", *Surv. Ophthalmol.*, Vol. 52, No.3, pp. 227–243, May-June, 2007.
- [26] P. A. Keane, P. J. Patel, S. Liakopoulos, F. M. Heussen, S. R. Sadda, and A. Tufail, "Evaluation of age-related macular degeneration with optical coherence tomography", *Surv. Ophthalmol.*, Vol. 57, No.5, pp. 389-414, Sept.-Oct., 2012.
- [27] K. Li, X. Wu, D. Z. Chen, and M. Sonka, "Optimal surface segmentation in volumetric images—a graph-theoretic approach," *IEEE Trans. Pattern Anal. Mach. Intell.*, Vol. 28, No. 1, pp. 119–134, Jan. 2006.
- [28] D. Hochbaum, "A new-old algorithm for minimum-cut and maximum-flow in closure graphs," *Networks*, Vol. 37, pp. 171-193, 2001.
- [29] J. Picard, "Maximal closure of a graph and applications to combinatorial problems", *Manage. Sci.*, Vol. 22, pp. 1268-1272, 1976.
- [30] X. Chen, J. K. Udupa, U. Bağcı, Y. Zhuge and J. Yao, "Medical image segmentation by combining graph cut and oriented active appearance models", *IEEE Trans. Image Process.*, Vol.21, No.4, pp. 2035-2046, Apr. 2012.
- [31] C. Tomasi, R. Manduchi, "Bilateral filtering for gray and color images", in *Proc. IEEE ICCV*, pp. 839–846, 1998.
- [32] S. Paris and F. Durand, "A fast approximation of the bilateral filter using a signal processing approach," *Int. J. Comput. Vision*, Vol. 81, No. 1, pp. 24–52, Jan. 2009.
- [33] J. K. Udupa, V. R. Leblanc, Y. Zhuge, C. Imielinska, H. Schmidt, L.M.Currie, B. E. Hirsch, and J. Woodburn, "A framework for evaluating image segmentation algorithms," *Comput. Med. Imag. Graphics*, Vol.30, No. 2, pp. 75–87, 2006.
- [34] N. Otsu, "A threshold selection method from gray-level histograms," *IEEE Trans. Syst., Man, Cybern.*, Vol. 9, No. 1, pp. 62-66. 1979.